International Journal of Hydrogen Energy 113 (2025) 535–549

Contents lists available at ScienceDirect

International Journal of Hydrogen Energy

journal homepage: www.elsevier.com/locate/he

Membraneless electrolyzer designed using the tesla valve concept for hydrogen production

Mohammadali Zoljalali, Richard Ahorsu, Francesc Díaz, Magdalena Aguiló, Xavier Mateos *

University Rovira I Virgili (URV), Physics and Crystallography of Materials (FiCMA), Marcel·lí Domingo 1, 43007, Tarragona, Spain

ARTICLE INFO

Keywords:
(Hydrogen
Membraneless electrolyzer
Microfluidics
Diodicity)

ABSTRACT

This study focuses on the fabrication of a membraneless electrolyzer using the Tesla valve concept. The designed electrolyzer by utilizing the fluidic forces and tesla valves concept separate the produced H_2 and O_2 without using a membrane. Elimination of the membrane contributes to increasing the flexibility of the working condition for the electrolyzers and decreases fabrication costs. Tesla valve membranelss electrolyzers can operate at a flow rate of 30 mL h^{-1} and a current density of 300 mA cm^{-2}. This pumping power is the lowest required pumping power for the reported current density in the literature of membraneles electrolyzers. Furthermore, by increasing the flow rate to 80 mL h^{-1}, this structure works at up to 600 mA cm^{-2}. Additionally, this study demonstrates that by leveraging the diodicity of the Tesla valve and changing the placement of the anode and cathode, the hydrogen production frequency can be increased by an average of 13%.

1. Introduction

Climate change is a consequence of the widespread use of fossil fuels as an energy source. Intensive research is now focused on identifying alternative energy vectors that can mitigate the negative impacts of climate change [1]. One of the key emerging alternatives to traditional energy sources is Hydrogen (H_2). H_2 has a higher gravimetric energy content (143 MJ kg^{-1}) than conventional petroleum fuel (50 MJ kg^{-1}), and its combustion products have zero carbon, thus making it attractive [2].

Electrolyzers are the most used devices for carbon-free H_2 production [3]. In this process, H_2 is produced through electrolysis, where electricity is used to split water into O_2 and H_2 [4,5]. Electrolyzers typically consist of three main components: two electrodes, an electrolyte, and a membrane or diaphragm [6]. In conventional water-splitting electrolyzers, a membrane (in PEM electrolyzers) or a diaphragm (in alkaline electrolyzers) separates the produced H_2 and O_2 [7]. However, these membranes and diaphragms introduce several challenges that reduce electrolyzer efficiency. Issues like degradability at high temperatures, O_2 leakage, and high maintenance costs have driven scientists to explore alternative electrolyzer configurations [8]. In gas-evolving reactions, such as total water electrolysis, the evolution of gaseous products including nucleation, coalescence, and detachment occurs at a much slower rate than reactant adsorption and electron transfer [9,10]. This disparity contributes to the blockage of active sites, leading to greater energy loss and increased ionic resistance [11,12]. Electrochemical energy conversion processes at the microscale offer a pathway to solving several challenges associated with standard electrolyzers. Microscale devices have found application in many sectors including electrochemical [13,14], and photocatalytic water splitting [15]. Microscale characteristics, such as channel length, width, depth, and interelectrode distance, improve temperature and concentration gradients [16]. Microreactors for electrolysis, with microscale electrode separation, also experience less ohmic loss, better material utilization, and higher energy density due to the enhanced transport of reactants, products, and charge ions. Electrochemical microreactors capitalize on the high surface-to-volume ratio to achieve superior reaction kinetics during chemical conversions at the electrode surface. These advantages of microreactors have drawn attention to the potential of leveraging microscale features in electrolyzer configurations, particularly in eliminating membranes (membraneless systems) [17,18]. Removing membranes reduces design complexity, increases practicality, and lowers fabrication costs.

As the name suggests, membraneless electrolysis devices do not require a membrane. Membraneless water electrolysis (MWE) devices utilize geometric and electrode microstructure designs to separate H_2 and O_2. Convection within channels or diverging flow fields helps

* Corresponding author.
E-mail address: xavier.mateos@urv.cat (X. Mateos).

https://doi.org/10.1016/j.ijhydene.2025.02.235
Received 16 October 2024; Received in revised form 19 January 2025; Accepted 14 February 2025
Available online 5 March 2025

Nomenclature

CO_2	Carbon Dioxide
H_2	Hydrogen
j	Current density (mA.cm^{-2})
M	Molarity (moles per liter, mol/L or M)
MWE	Membraneless Water Electrolysis
O_2	Oxygen
P	Pressure (Pa)
PDMS	Polydimethylsiloxane
PEM	Proton Exchange Membrane
PFOS	Perfluorooctanesulfonic Acid
Re	Reynolds Number
RIE	Reactive Ion Etching
TVME	Tesla Valve Membraneless Electrolyzer
Um	Mixture velocity (m.s^{-1})
$(Um)^T$	Transpose of the mixture velocity vector
UV	Ultraviolet
V	Voltage (V)
μ_m	Mixture viscosity (Pa·s)
ρ_m	Mixture density (kg.m^{-3})

separate dissolved or two-phase gases produced at the cathode and anode. These designs include Flow-by and Flow-through configurations, both of which employ fluid dynamics for efficient gas separation without the need for membranes.

Flow-by and Flow-through configurations have demonstrated potential for operating at high current densities, with production costs comparable to conventional electrolyzers [8]. The techno-economic analysis of membraneless electrolyzers indicates a levelized cost of H_2 at approximately 2 USD. kg^{-1} H_2, rivaling steam reforming and showing significantly higher profitability than conventional electrolyzer technologies [19]. However, product separation remains a challenge for membraneless electrolyzers due to the lack of a membrane or separator [20]. Research is ongoing into bubble growth at the electrode and

Table 1
Dimensions of Parallel Electrode electrolyzers and Tesla Valve electrolyzers.

Parameter	Dimensions [μm]
Working electrode surface area	1.485×10^5 μm^2
Inter electrode distance	710 μm
PE electrolyzer channel width	800 μm
TVME electrolyzer channel width	200 μm
Wd (TVME electrolyzer tesla connector width)	40 μm
Da	290 μm
Db	96 μm
Dc	55 μm
Dd	50 μm
θ	28^O

movement within the channels to address this issue [6,21–25]. Bubble coalescence and detachment from the electrodes result in the formation of larger bubbles, which can lead to gas crossover [10].

The addition of surfactants to the electrolyte reduces surface tension, leading to the detachment of smaller bubbles [26]. In one study, a three-channeled membraneless electrolyzer achieved only 0.14% H_2 crossover at an 80 mL h^{-1} flow rate and 300 mA cm^{-2} current density 58 times lower than conventional membraneless electrolyzers [27]. Adding a perfluorooctanesulfonic acid (PFOS) surfactant further reduced H_2 crossover by 21% and decreased overpotential by 1.9% by improving bubble dynamics [27]. The presence of Triton X-100 surfactant in an electrolyte has been found to prevent bubble coalescence, speed up bubble detachment, improve product separation, and reduce ohmic resistance at lower flow rates (Reynolds number, Re = 10) during an electrochemical event [28]. However, surfactant use poses challenges in large-scale applications.

(i) The need for surfactants increases the complexity of electrolyzer maintenance, raising operational costs.
(ii) Different surfactants are incompatible with specific electrode materials, leading to potential compatibility issues.
(iii) Interactions between surfactants and the electrolyte may affect ionic conductivity, pH balance, or result in the formation of unwanted byproducts.

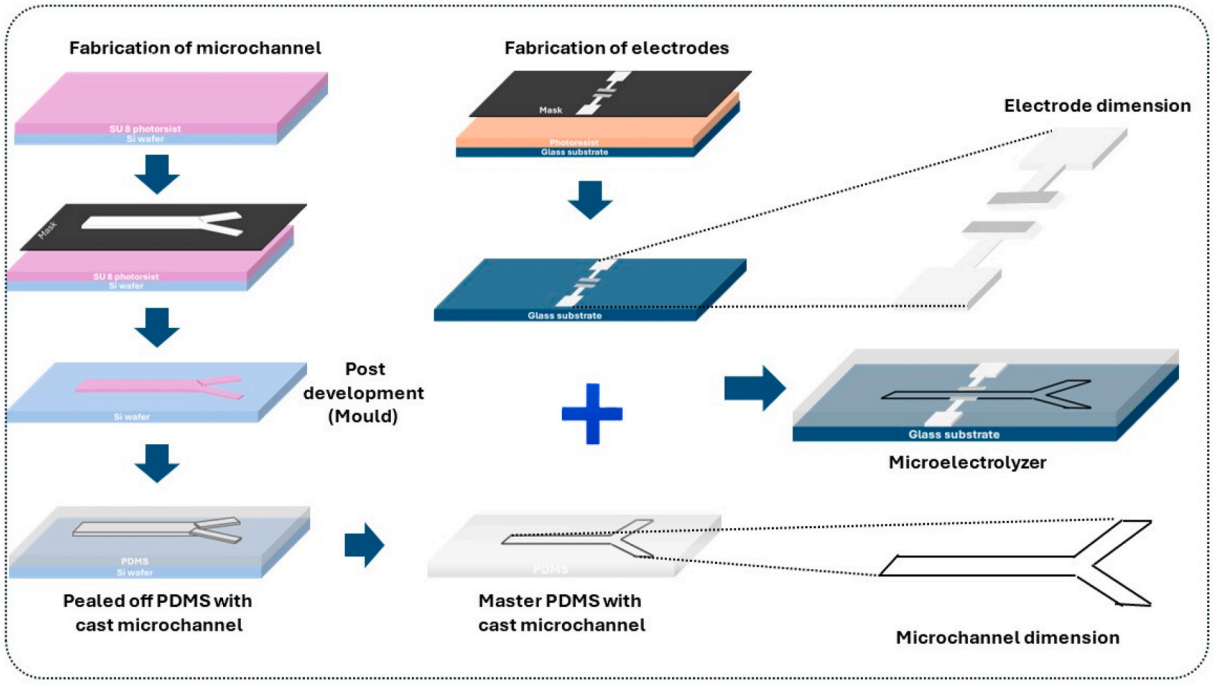

Fig. 1. Micro electrolyzer fabrication process.

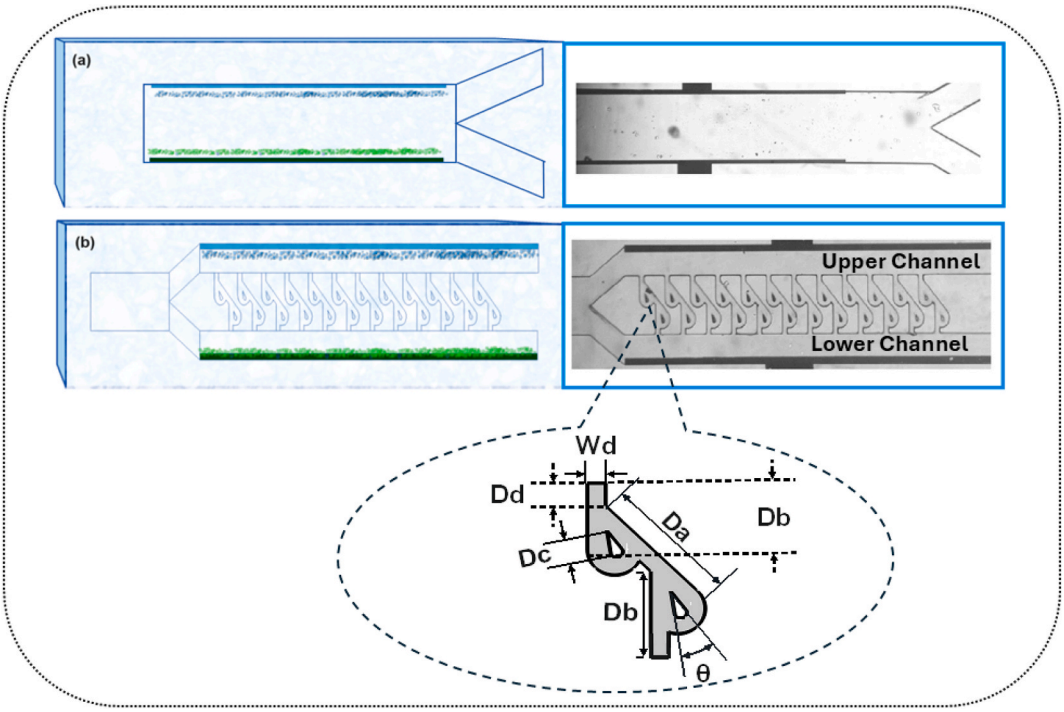

Fig. 2. a. Parallel electrode electrolyzer b. Tesla Valve electrolyzer.

A further drawback of membraneless reactor design is the occurrence of backpressure events or backflow of electrolyte due to flow rate fluctuations caused by unstable functioning pumps. These events cause bubbles to saturate at the electrode, slowing H_2 production.

Here, we present a state-of-the-art design for a membraneless electrolyzer based on the Tesla valve concept. The working principle of the Tesla valve involves two parts: (i) the main straight channel and (ii) a branched arm; see Fig. 2b. It has a split channel that rejoins the main flow channel perpendicularly when the flow reverses direction. The primary channel transports the majority of the flow in the forward direction with minimal pressure loss [29,30]. The Tesla Valve Membraneless Electrolyzer (TVME) relies solely on its geometry to create flow resistance, favoring one direction over the other. The TVME consists of a series of interconnected channels that direct the flow, allowing it to move easily in one direction while creating obstacles and increased resistance in the reverse direction. It is desirable to speed up the detachment of the bubbles from the TVME to improve its efficiency. A better understanding of bubble flow phenomena in channels via simulation allows the development of robust TVME to reduce the overpotential at the electrodes, which assists the improvement of mass transfer during electrochemical reactions [31].

Our objectives in this study are.

(i) To evaluate the H_2 production of the TVME and a Parallel Electrolyzer (PE) as a control.
(ii) To assess the geometric capability of the TVME to use its inherent forced convection for maintaining a steady supply of electrolyte to the electrodes, while detaching and separating the generated gases from the electrode surface.
(iii) To optimize the interconnected channels of the TVME via computational simulations to enhance convective flow and calculating bubbles plume thickness
(iv) To calculate the diodicity. It quantifies how effectively the TVME restricts reverse flow compared to forward flow. This measurement will then be used to manipulate electrolyte circulation, thereby increasing the H_2 production rate.

To the best of our knowledge, this is the first time the Tesla valve-driven microreactor concept has been applied to H_2 generation. Our work sets the foundation for scaling up microfluidic structures into pilot systems and advancing to higher technology readiness levels (TRL).

2. Experimental setup

The membraneless electrolyzer fabrication has two distinct sections. Fig. 1 shows the fabrication process. First the electrode part was fabricated with sputtering. One microscope glass was coated with AZ15015 using a Spin coater. Then after treatment, it was exposed by UV radiation through the mask with the electrode design. After development of the sample, the sputtering process has been going ahead and the 10 nm titanium and 100 nm platinum was sputtered on the glass.

Parallelly, one silicon wafer was coated by SU82035, and after coating it was baked. Subsequently, it has been exposed to the UV with photomask with the channel design. After exposure and post baking, the wafer developed to have the final mold. Once the mold was prepared, polydimethylsiloxane (PDMS) mixture was poured on the mold and put it in the oven for 1 h at 80 °C to be solidified. After having the channel, glass slide with the electrode and the PDMS channel were bonded together by Reactive Ion Etching (RIE)-Oxford.

In the experimental part, the membraneless electrolyzer was connected to a pump (Elveflow OB1 MK4) to pump the 0.5 M sulfuric in the range of 30 mL h^{-1} to 80 mL h^{-1} acid solution as electrolyte within the device in room temperature. A potentiostat (Ivium Vertex. C) was utilized to apply the voltage necessary for initiating water splitting in current densities between 75 mA cm^{-2} to 600 mA cm^{-2}. To study and characterize the electrolysis process, a high-speed camera (Optronis CR600x2) capable of capturing videos at 7000 frames per second (fps) was employed. The bubbles behavior was analyzed by using these recorded videos along with Python code. The mentioned code first converts the videos to frames and convert them to gray scale. Then after denoising the pictures the Hough Circle Transform is used to find circular shapes (bubbles) within the specified ROI. Detected circles are then drawn on the frame, and their information is stored for further analysis. For precise analysis of the output gas, two test tubes - both side

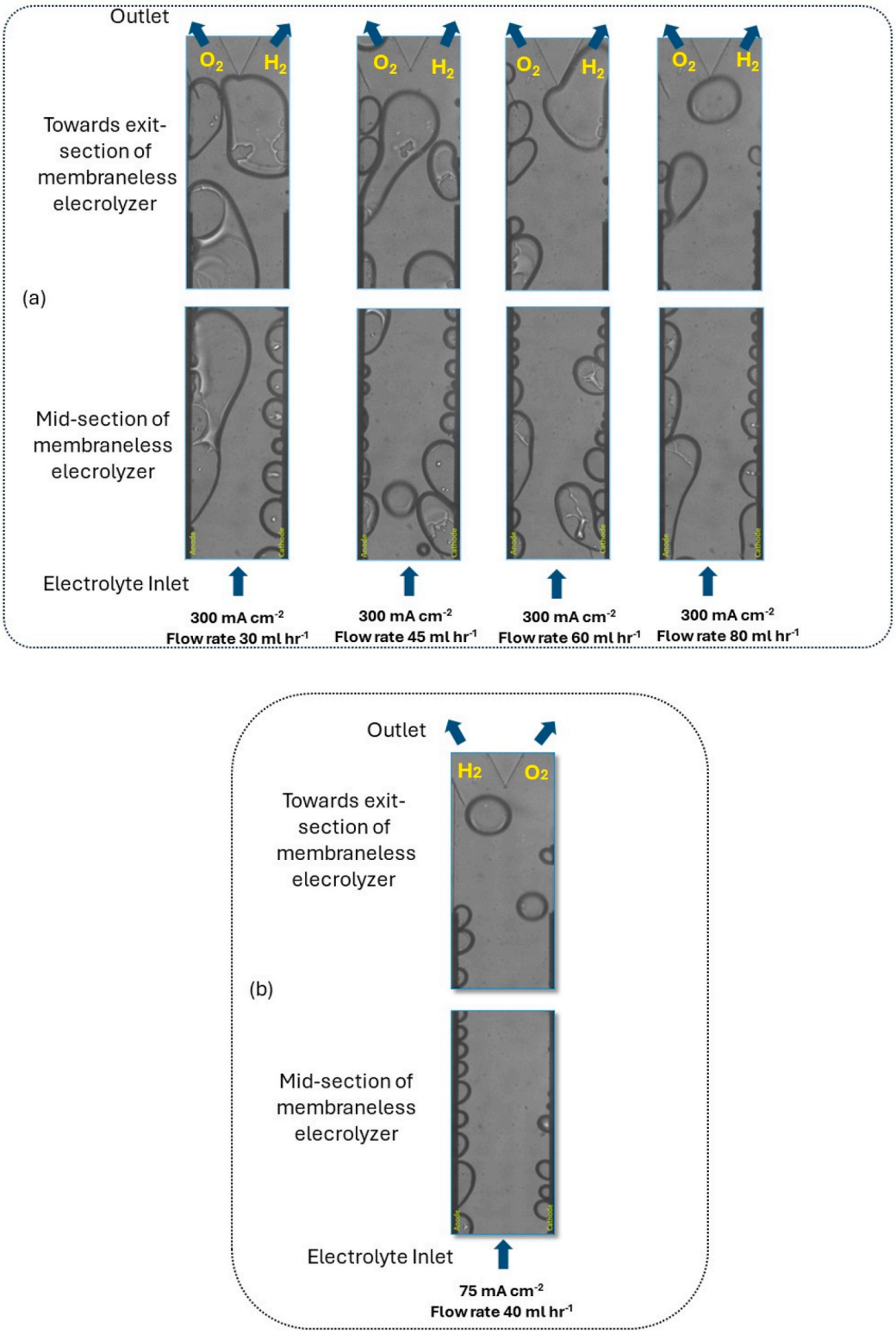

Fig. 3. Visualization of bubble generation at parallel electrode (a) 300 mA cm^{-2} at different flow rates, 30 mL h^{-1}, 45 mL h^{-1}, 60 mL h^{-1}, 80 mL h^{-1}, and electrolyte 0.5 M H_2SO_4. (b) 75 mA cm^{-2} at flow rate of 45 mL h^{-1}.

open-were covered with septum caps and fill with electrolyte. These tubes were held inversely in a larger container of same electrolyte. The produced H_2 and O_2were collected for 30 min separately in these tubes. All the experiments were repeated for 3 times. An airtight syringe was used to retrieve the collected gases from the tubes. The gases were injected into Shimadzu Nexis GC-2023 gas chromatograph model fitted with a thermal conductivity detector for H_2 and O_2 crossover determination. N_2 gas was used as a carrier gas. All experiments were repeated 3x.

3. Results and discussion

In this study, two distinct geometries are examined and depicted in Fig. 2. Dimensions of both structures feature is listed in Table 1 the same

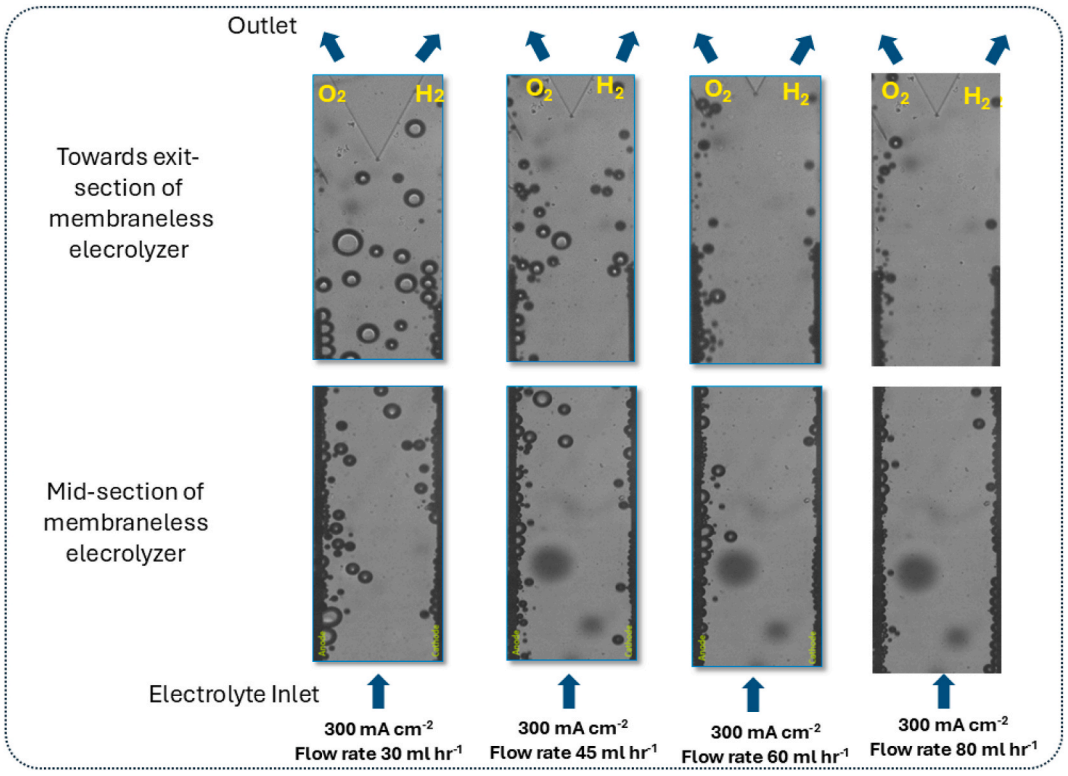

Fig. 4. Visualization of surfactant effects on bubble generation at parallel electrode (Parallel Electrolyzer); at working conditions, current density, j = 300 mA cm^{-2} at different flow rates, 30 mL h^{-1}, 45 mL h^{-1}, 60 mL h^{-1}, 80 mL h^{-1}, and electrolyte 0.5 M H_2SO_4 + TritX.

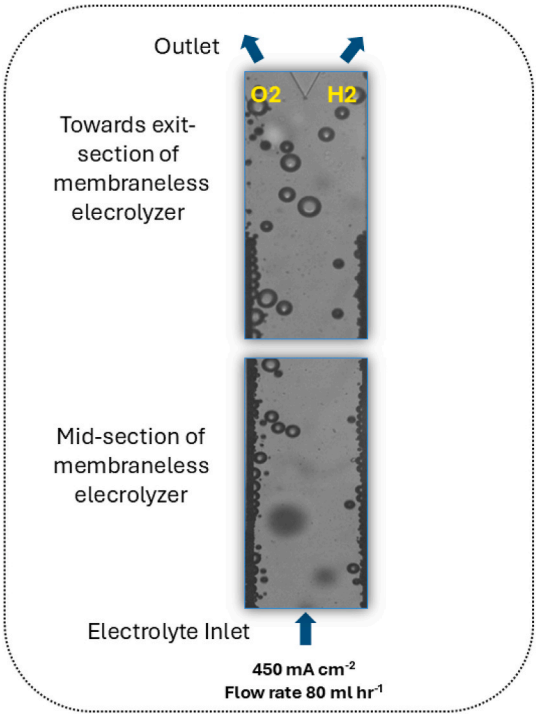

Fig. 5. Bubble generation at parallel electrodes (Parallel Electrolyzer); at the working conditions; current density, j = 450 mA cm^{-2} 80 mL h^{-1}, and electrolyte 0.5H2SO4 + TritX.

working platinum electrode surface area and inter electrode distance is used for both structures. The first part of the study will focus on the parallel electrode configuration, followed by an analysis of a new geometry incorporating a Tesla valve design.

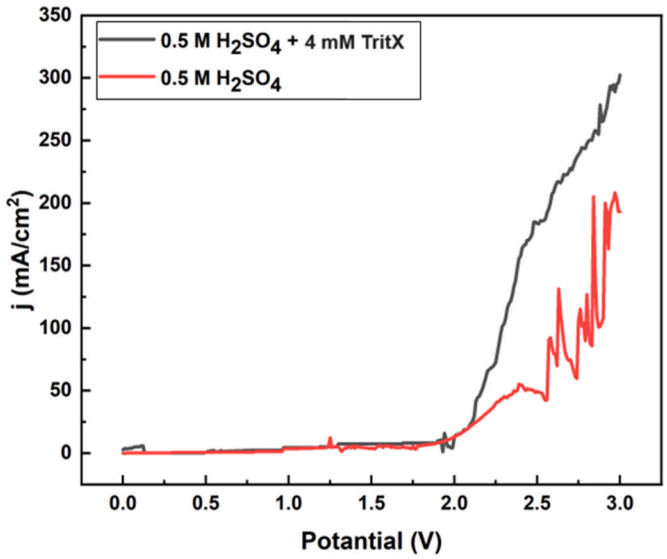

Fig. 6. Linear Sweep Voltammetry for PE Electrolyzer for 0.5 M H_2SO_4 and 0.5 M H_2SO_4 +4 mM TritX. The scan rate is 100 mV S^{-1}.

3.1. Parallel electrode electrolyzer

The parallel electrode (PE) electrolyzer depicted in Fig. 2a utilizes fluidic force to separate the produced H_2 and O_2 gases. This phenomenon is explained by the Segre-Silberberg principle [32], where bubbles achieve an equilibrium position based on their size and flow rate. By adjusting these parameters, bubbles can be effectively separated [33].

Fig. 3 illustrates water splitting in a simple channel with parallel electrodes employing 0.5 M H_2SO_4 electrolyte. Fig. 3a shows that at 300 mA cm^{-2}, bubbles detachment radius decreases by increasing the flow

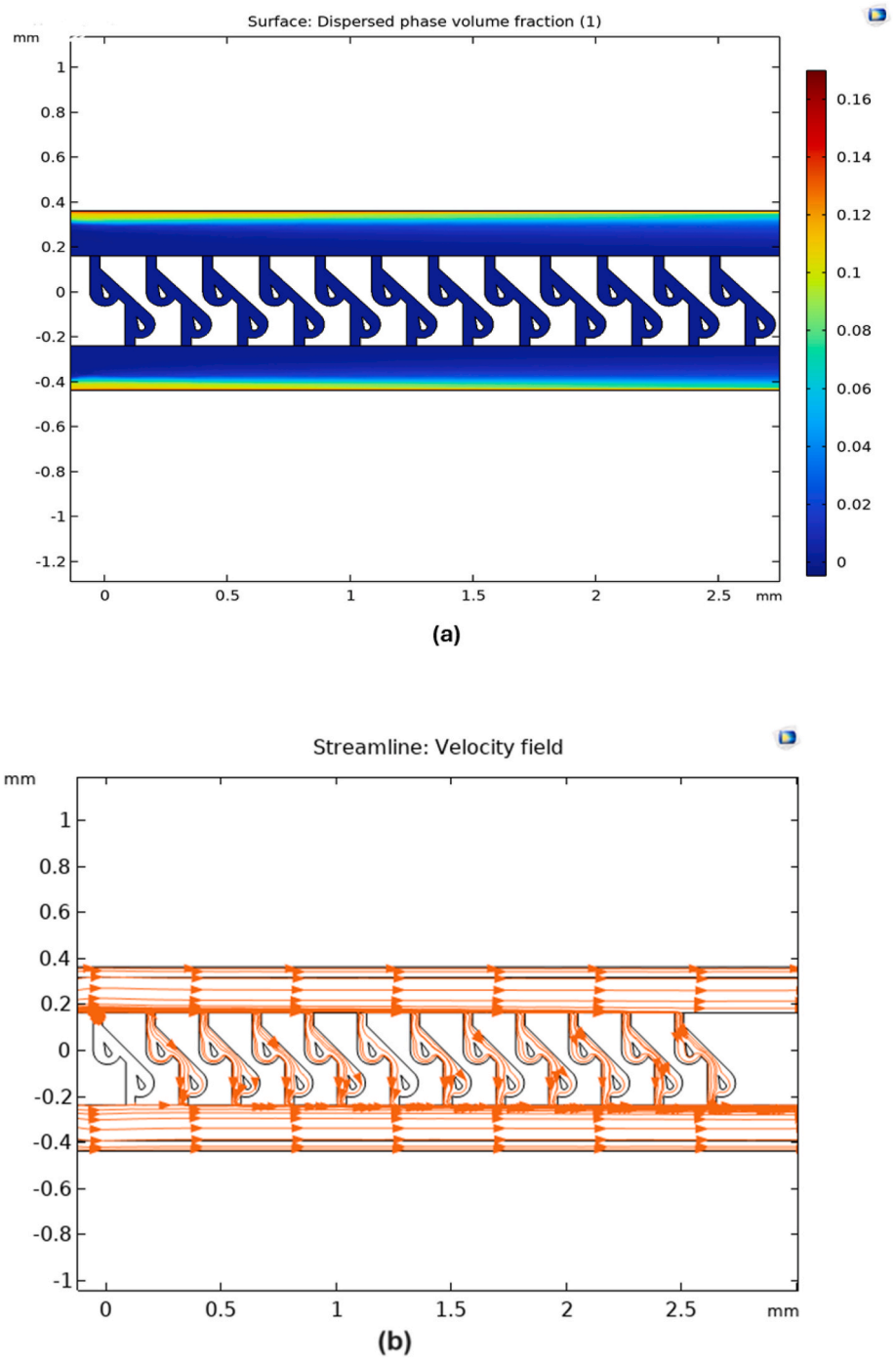

Fig. 7. Simulation results for the (a) volume fraction (b) Streamline of the velocity field.

rate. At lower flow rates, bubble detachment is delayed, causing bubbles to grow and potentially cross to the other side of the channel, leading to H_2 and O_2 crossover. Additionally, the coalescence of larger bubbles can block the output, worsening the situation. Fig. 3b shows that this system can work up to 75 mA cm^{-2} and flow rate of 45 mL h^{-1} with some perfect separation.

From Fig. 3, it was evident that increasing the flow rate from 30 mL h^{-1} to 80 mL h^{-1} at 300 mA cm^{-2} prevented bubble crossover and also contributed to the early detachment of bubbles in PE. It was observed that oxygen gas bubbles are nucleated less frequently than hydrogen bubbles, and the size of the hydrogen bubbles are usually smaller than the size of the oxygen bubbles. In the system oxygen bubbles adhere more strongly to the electrode [34]. Electrostatic repulsion force between the negative cathode and the hydrogen bubbles are other factors that contribute to smaller bubble size of the hydrogen [35] However, it requires high pumping power to reach a flow rate of 80 mL h^{-1}. Using excessive pumping power is undesirable from an optimization point of view [36]. Surfactant was added to the electrolyte to circumvent the bottleneck caused by increased pumping power.

In the presence of surfactant (Triton X), with a flow rate of 30 mL h^{-1} and j = 300 mA cm^{-2}, crossover of O_2 and H_2 occurred; see Fig. 4. The crossover of gases decreased significantly at elevated flow rates (60 and 80 mL h^{-1}) in comparison to the crossover observed with the surfactant-free electrolyte set-up in Fig. 3. It was evident that at flow rate above 60 mL h^{-1} the crossover was almost zero. Additionally, the presence of the surfactant reduced the diameter of the bubbles, promoted early

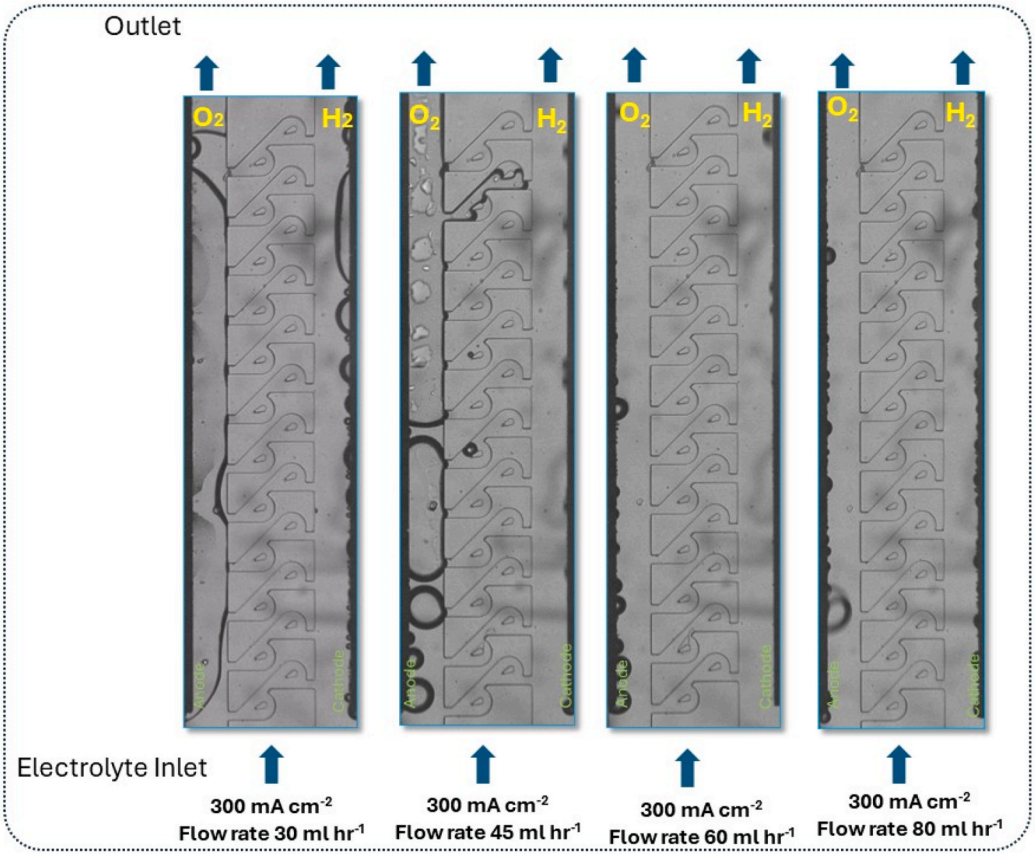

Fig. 8. Bubble generation in TVME at j = 300 mA cm^{-2} for various flow rates; 30 mL h^{-1}, 45 mL h^{-1}, 60 mL h^{-1}, and 80 mL h^{-1} using 0.5 M H_2SO_4.

detachment of bubbles and averted bubble coalescence.

To test for the impact of current density on bubble size dynamics in the presence of surfactants, we increased the current density to 450 mA cm^{-2}. At j = 450 mA cm^{-2}, the bubbles appeared to be apart at the midsection of the PE but eventually coalesced at the exit section; see Fig. 5. This observation is consistent with the literature [27].

Fig. 6 displays the polarization curve for the PE electrolyzer. A sharp polarization curve was recorded when surfactant was added to the electrolyte. Large bubbles in the channel and on the electrode surface contribute to potential loss. The addition of surfactant to the electrolyte aided the bubbles to detach at a smaller diameter as a result of limited Coulombic forces caused by the adsorption of charged surfactant molecules on the bubble and electrode surface [10].

The surfactant in the electrolyte minimizes the surface tension. Thus, the composition of the electrolyte affected bubble properties, thereby causing the sharp polarization curve to be recorded [37].

Despite adding surfactants might reduce bubble-induced energy losses, it complicates the process because these molecules may participate in electrode processes [10]. Considering this limitation, we fabricated TVME as a novel approach to investigate its geometrical properties on bubble separation, bubble detachment, and H_2 production.

3.2. Tesla valve membranless electrolyzer

In the Tesla valve membranless electrolyzer (TVME), the Tesla valve concept has been incorporated into design as depicted in Fig. 1b. TVME consists of two main channels that host the anode and cathode at outer sidewalls of each channel. The two channels are interconnected by some Tesla valves. These connections establish ion transfer, which is needed for starting the water splitting and H_2 production. The difference in the size of these channels and connectors, accompanied with variation in fluid velocity eases the bubbles separation. The Tesla structure allows for manipulation of electrolyte flow and ion transfer as well [38].

The bubbles generated at electrodes do not tend to move towards the Tesla connectors in TVME as this is not energetically favorable during water splitting event. This phenomenon occurs as results of the bubbles' effort to minimize their surface energy. However, the bubbles can grow big enough to block the output occasionally thereby causing the bubbles to enter the Tesla connectors.

To gain a better understanding of bubble behavior, studying fluid flow and the thickness of the electrode gas plume would be beneficial. To achieve this aim, Mixture Model for multiphase flow in COMSOL Multiphysics software has been solved [39].

The Mixture Model, applying Laminar Flow interface solves one set of Navier-Stokes equations for the momentum of the mixture [40]. The pressure distribution is calculated from a mixture-averaged continuity equation while the velocity of the dispersed phase is described by a slip model. The volume fraction of the dispersed phase is tracked by solving a transport equation for the intended or specific to the volume fraction. This approach is a reasonable approximation for small electrochemical bubbles that have a lower density than that of the electrolyte. This module efficaciously simulates the behavior of small bubbles produced by water splitting given the bubble's smaller density in comparison with the electrolyte. The continuity and momentum equations at steady state are equations (1) and (2), respectively.

$$\nabla.\left(\rho_m U_m\right) = 0 \tag{1}$$

$$\rho_m U_m \nabla U_m = -\nabla p + \nabla.\left(\mu_m\left(\nabla \mathrm{U}_m + (\nabla U_m)^T\right)\right) \tag{2}$$

Considering the mixture model, a no-slip condition was applied to the electrode section of the mixture. In equations (1) and (2), $\rho_{m,}$, U_m and μ_m denote mixture density, mixture velocity and mixture viscosity, respectively.

The results, depicted in Fig. 7, show the dispersed phase volume

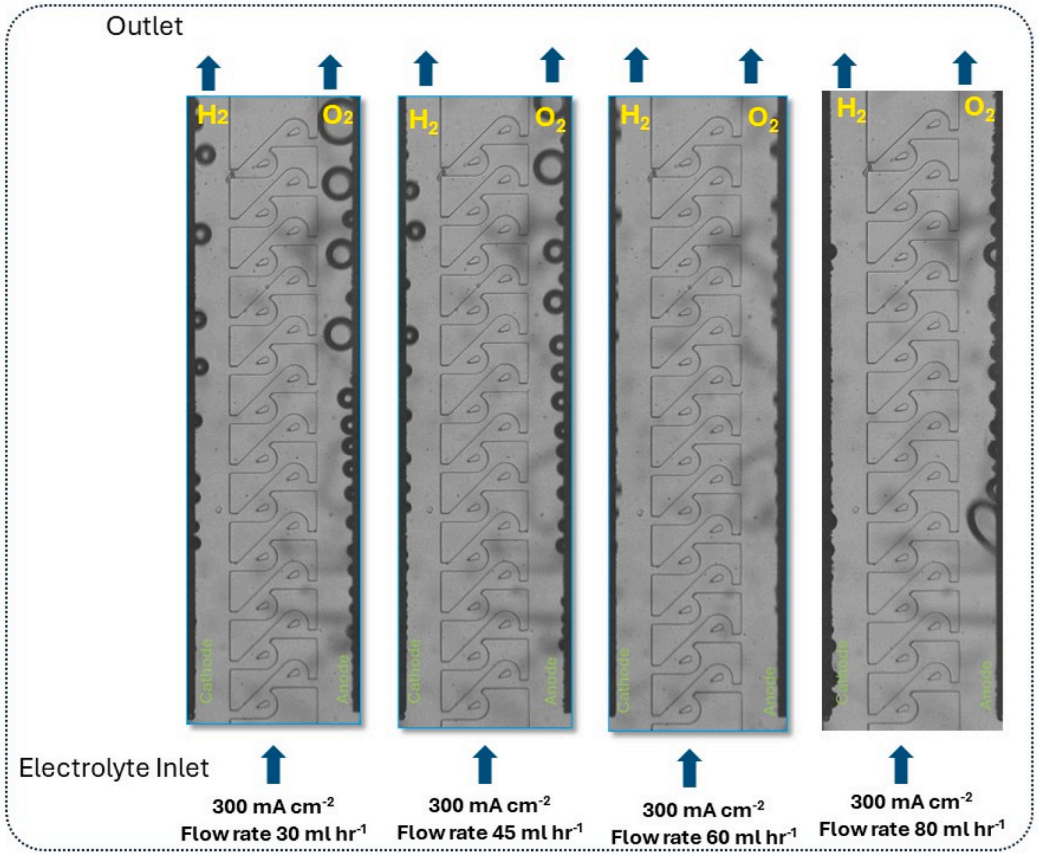

Fig. 9. Bubble generation in TVME at 300 mA cm^{-2} for various flow rates; 30 mL h^{-1}, 45 mL h^{-1}, 60 mL h^{-1}, and 80 mL h^{-1} using 0.5 M H_2SO_4.

fraction and velocity field. In Fig. 7a the dispersed phase is Hydrogen and Oxygen. Simulation results indicate that, at a specified current and flow rate the bubble plume is approximately 100 μm [41]. This indication is important, as reducing channel width causes reduction in ohmic losses. However, at certain point, elevated gas plume thickness may contribute to severe crossover. Appendix I provides a detailed explanation of the simulation. Fig. 7b illustrates the streamline of the velocity field in TVME and demonstrates the direction of the fluid flow in the tesla connections. As observed, electrolyte flows from the upper channel to the lower channel, and streamlines in lower channel have a higher density. The simulation results show that average flow rate in the tesla connection is ten times smaller than the main channel.

Fig. 8 illustrates the water-splitting process in the TVME. Bubble generation was observed at a current density of j = 300 mA cm^{-2} using 0.5 M H_2SO_4. At lower flow rates of 30 mL h^{-1} and 45 mL h^{-1}, the electrochemical process stopped. This is due to the produced bubbles coalescing and growing to an elongated shape. The elongated bubbles distorted the expected ion transfer within the system; see Fig. 8, flow rate: 30 mL h^{-1} and 40 mL h^{-1}. At elevated flow rates, bubbles with smaller diameters were generated and detached faster from electrodes, see Figs. 8 and 60 mL h^{-1}, 80 mL h^{-1}.

Fig. 9 presents TVME under identical experimental conditions as in Fig. 8, yet switched the polarization at the electrodes (the anode in Fig. 8 became the cathode in Fig. 9, and vice versa for the cathode in Fig. 8). At applied j = 300 mA cm^{-2}, bubbles generated at both cathode and anode had smaller diameters with faster detachment regimes at lower flow rates of 30 mL h^{-1} and 40 mL h^{-1}, hence establishing the superiority of TVME over PE in a surfactant-free context. This result can be explained by the concept of diodicity, which refers to the ability of a microvalve to allow flow in the forward direction while inhibiting flow in the reverse direction [42]. The lower channel aided by the diodicity of the Tesla connectors, experiences a higher flow rate, which effectively removes the O_2 generated. It was observed that bubbles at the cathode had a smaller diameter in comparison to bubbles generated at the anode across various flow rates; see Fig. 9 [43,44]. This difference arises from H_2's smaller density and lower total negative body force. This force is decisive in detachment diameter [34,35,45].

We evaluated the gas evolution in the presence of surfactant in TVME under different electrode polarity configurations; see Figs. 10 and 11. It was observed that the changes of polarity at electrodes did not affect the characteristics of bubbles as evident in the surfactant-free setup. On the other hand, the rate of gas production increased when surfactant was added to the electrolyte; see Figs. 10 and 11. The bubbles were also characterized with smaller diameters; see Figs. 10 and 11. It was expected that ramping the current density to 600 mA cm^{-2} would increase the production of gases generated at both electrodes, as demonstrated in Fig. 10b.

Fig. 12a shows the polarization curve for the TVME, demonstrating the effect of the surfactant on the performance of the electrolyzer. Fig. 12b illustrates the applied voltage deviation required to operate at 300 mA cm^{-2}. The range of deviation in lower flow rate is due to the presence of bubbles [20,46]. At higher flow rates, the bubbles detach easily with smaller diameter. Fig. 12c presents the H_2 crossover for different flow rate and current density in the TVME. Values below the 4% H_2 concentration are within the non-explosive range. This figure shows that by adding the surfactant to the electrolyte, the TVME can work at 30 mL h^{-1} and j = 300 mA cm^{-2}. Moreover, it shows that TVME structure can operate at j = 600 mA cm^{-2} under conditions where the flow rate is 80 mL h^{-1}, and the electrolyte contains surfactant. The required potential for at j = 600 mA cm^{-2} is reported in Fig. 12b. The calculation of the Reynolds number for the TVME, considering a 400 μm × 100 μm inlet channel, reveals that TVME can operate at a Reynolds number of 33.3 and a j = 300 mA cm^{-2}. This represents the lowest pumping power reported in the literature to achieve complete

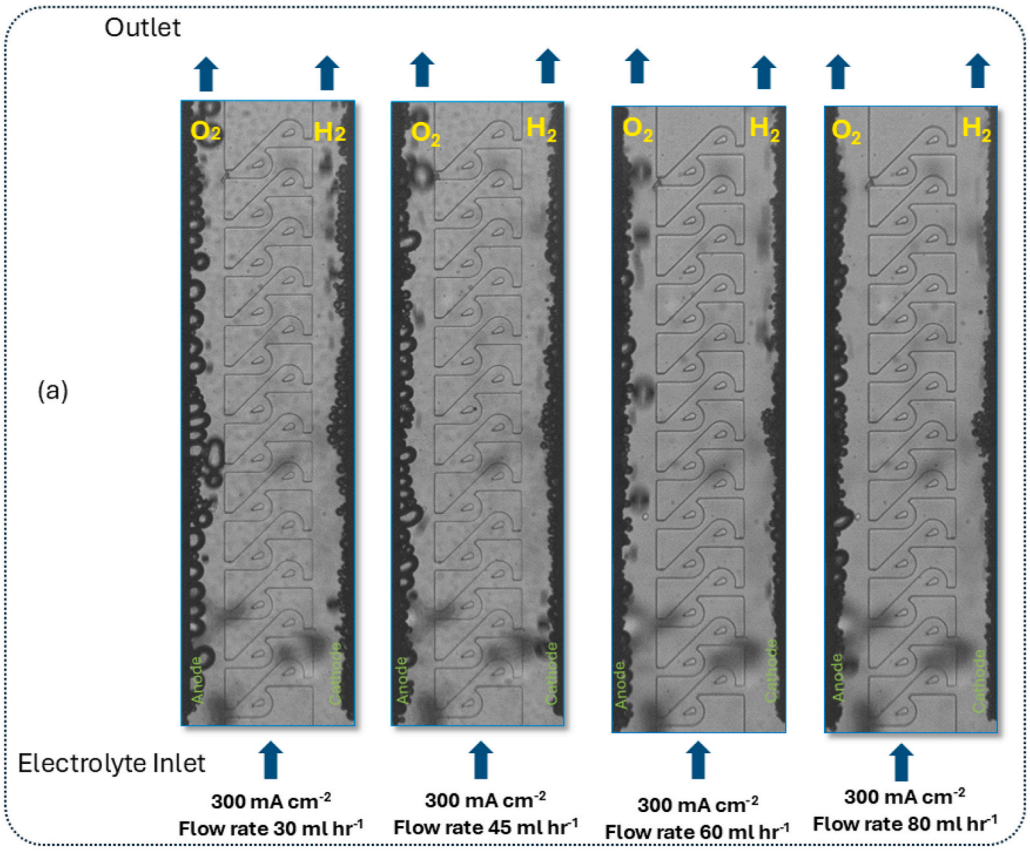

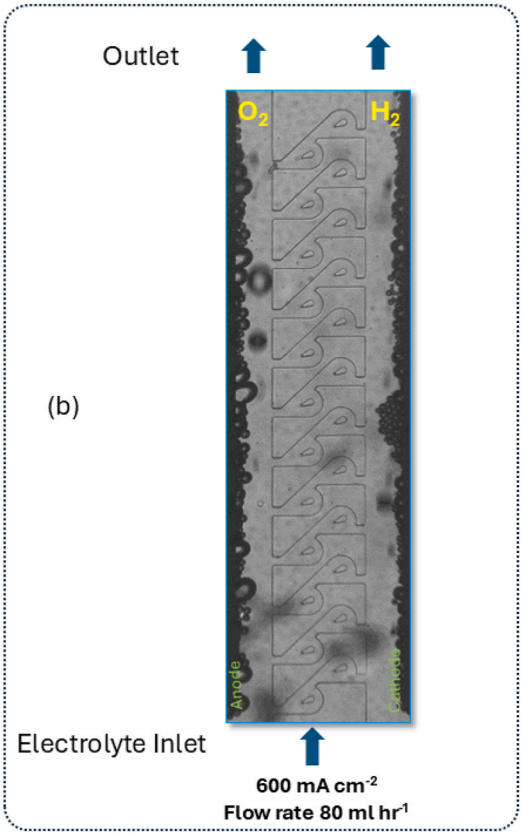

Fig. 10. (a) Bubble generation in TVME at j = 300 mA cm^{-2} various flow rates; 30 mL h^{-1}, 45 mL h^{-1}, 60 mL h^{-1}, and 80 mL h^{-1} using 0.5 M H_2SO_4, +4 mM TritX. (b) 600 mA cm^{-2} at 80 mL h^{-1} using, 0.5 M H_2SO_4 + 4 mM TritX.

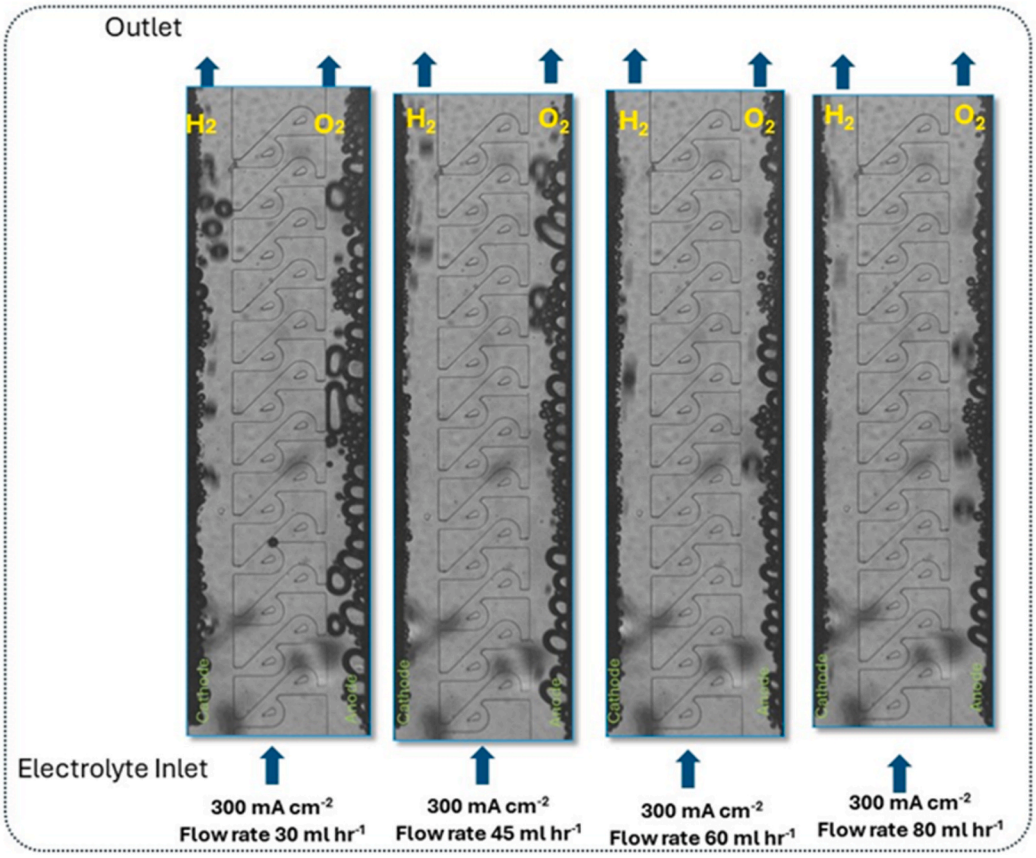

Fig. 11. Bubble generation in TVME at 300 mA cm^{-2} with different flow rates; 30 mL h^{-1}, 45 mL h^{-1}, 60 mL h^{-1}, and 80 mL h^{-1} using 0.5 M H_2SO_4 + 4 mM TritX.

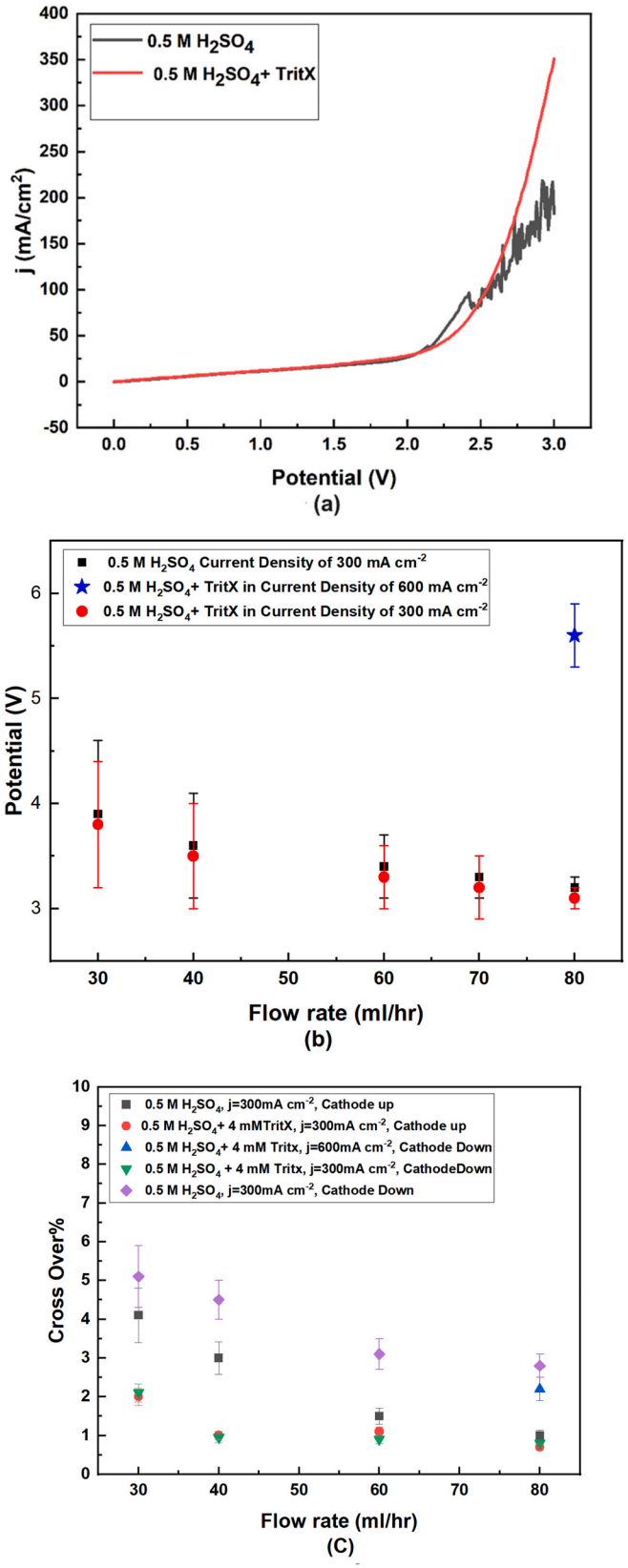

Fig. 12. (a) Linear Sweep voltammetry for the TVME with 0.5 M H_2SO_4 and 0.5 M H_2SO_4 + TritX. The scan rate is 100 mV S^{-1}, (b) Applied potential at a constant current density of 300 mA cm^{-2} with different flow rate; 30 mL h^{-1}, 45 mL h^{-1}, 60 mL h^{-1}, and 80 mL h^{-1} Applied potential at a constant current density of 600 mA cm^{-2} at flow rate of 80 mL h^{-1}. The bars indicate the standard deviation of the potential in a 6-min experiment. (c) Gas Chromatography results for flow rates; 30 mL h^{-1}, 45 mL h^{-1}, 60 mL h^{-1}, and 80 mL h^{-1}, current density j = 300 mA cm^{-2}, and electrode configurations (switching polarity between cathode and anode electrodes).

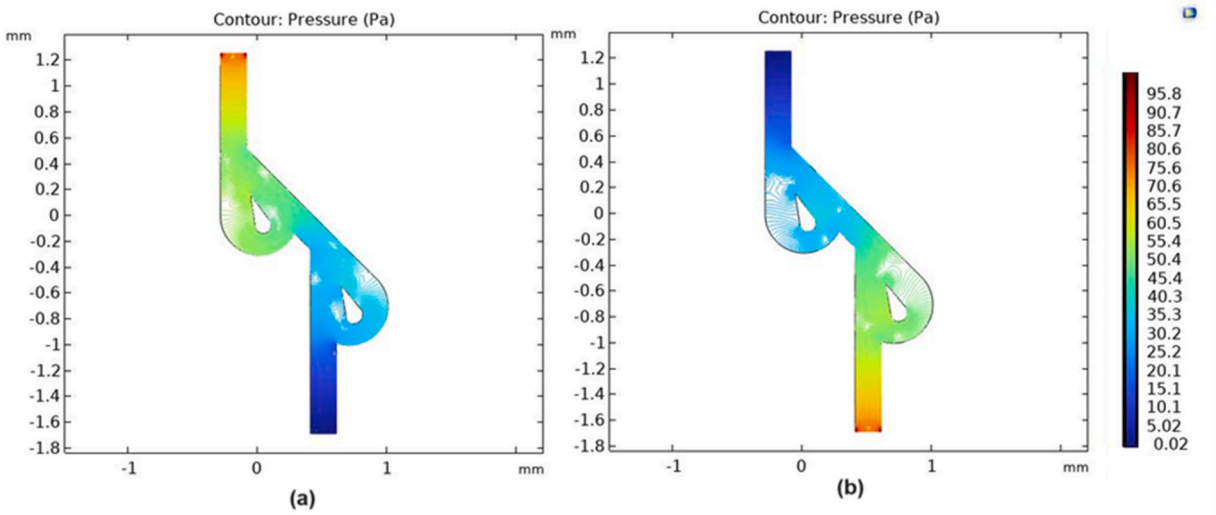

Fig. 13. Pressure counter (a) forward flow (b) reverse flow.

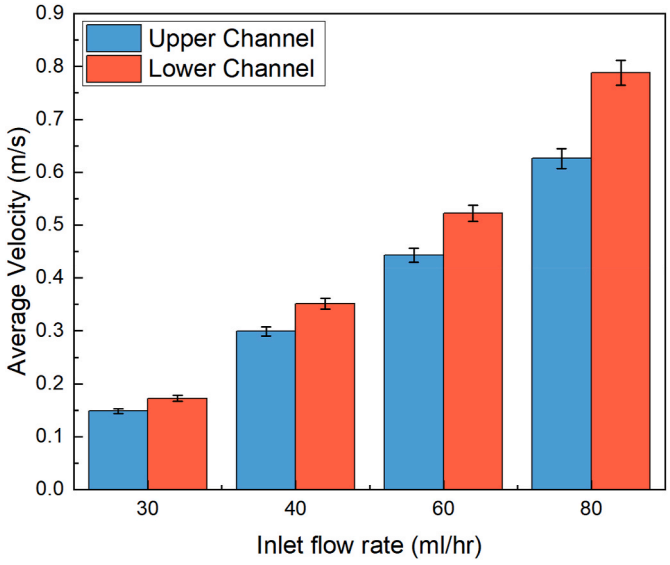

Fig. 14. Average H_2 bubbles velocity in upper and lower Channel.

separation of the produced H_2 and O_2 without the use of surfactants at the specified current density [27]. Additionally, the TVME can function at a current density of 600 mA cm^{-2} with a Reynolds number of 80, which aligns with the operating conditions of the porous wall (PW) electrolyzer as reported elsewhere [27].

3.3. Diodicity effect

The Tesla valve used in the electrolyzer can be considered as a one-way valve. With this design, increased convection enhances mass transport and reduces concentration polarization near the electrodes, potentially improving the system efficiency. Faster transport of electrolyte to the electrode surface replenishes reactants more rapidly thereby aiding, higher reaction rates. Additionally, the ion transfer between the two sides of the channel differs [47].

In electrochemical reactions, there are three mechanisms for ion transfer [17] diffusion, migration and convection. Since the TVME works as a one-way valve, convection is eliminated on one side. The diodicity of one of these valves has been shown in Fig. 13. The calculation of the diodicity indicates that it is slightly more than one. Therefore, the Tesla connections direct the electrolyte flow from the upper to the lower channels. This trend also can be observed in Fig. 7b as well.

Calculating the average velocity of bubbles in the upper and lower channels confirms that the electrolyte has higher flow rate in the lower channel. Fig. 14 illustrates the average velocity of the H_2 bubbles in both the lower and upper channel. These results confirm that the flow rate is higher in the lower channel. The data was extracted from a recorded video of the TVME with different flow rates. The calculation was repeated for three distinct experiments. The trend for O_2 bubbles is consistent.

Analyzing the output bubbles located at the exit section of TVME revealed the effect of diodicity on the production of bubbles. As it can be seen in Fig. 15, the electrode produced H_2 with higher frequency when convection ion transfer mechanism took place in the lower channel. Analyzing the bubble production rate in the lower and upper channels with python code and output videos shows that utilizing lower channel for the H_2 production contribute to 13% increase in the H_2 production frequency.

The acceleration of the H^+ transfer, improves mass transfer and lead to frequent bubble formation and faster detachemnt. This phenomenon contributes to increase in the active available surface of electrode, reducing coverage and allowing for a higher effective active area for the electrochemical reaction. As a result, while the total hydrogen volume produced remain constant with the applied current, the system operates with lower overpotentials, reduced concentration polarization, and improved overall efficiency, due to the higher production frequency.

The videos and code compiled for diodicity analyses are available in Supplementary material. This increase represents the average value for the four flow rates, 30 mL h^{-1}, 40 mL h^{-1}, 60 mL h^{-1}, and 80 mL h^{-1}, being evaluated by using the upper channel as a target parameter for the H_2 generation. The Python code processes each frame, and applies Hough Circle detection to identify bubbles (circles) within the ROI. The detected bubbles are drawn on the frame in green. For each detected bubble, the code stores its position (X, Y), radius, and the time step (based on the frame rate) in a list. The data of the hydrogen in different flow rates and for different polarization was considered. The output of upper and lower channel was studied in a specified timeframe and detected bubbles has been reported in Fig. 15.

4. Conclusion

Herein, we demonstrate a novel application of Tesla valve-based

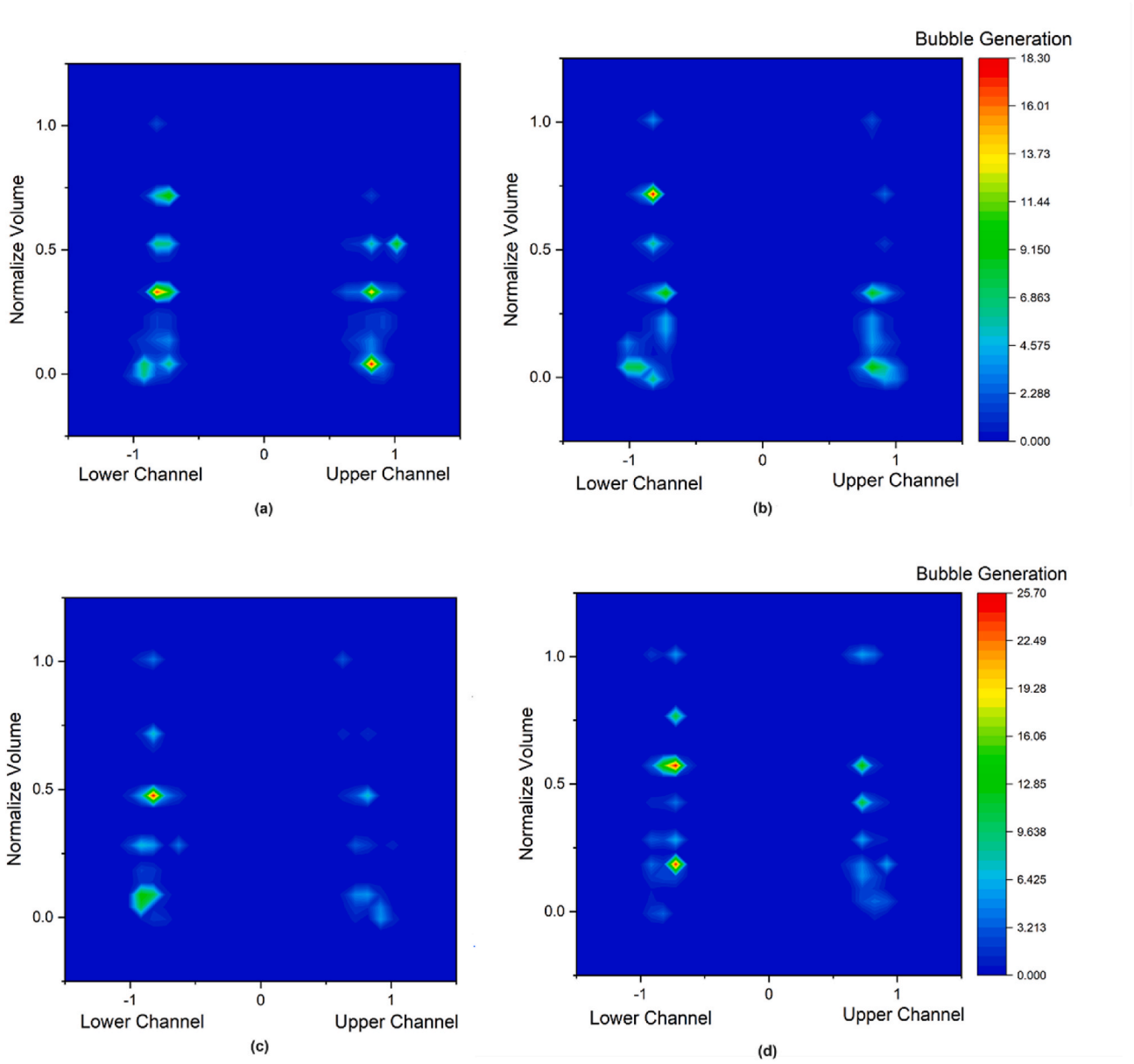

Fig. 15. H_2 production frequency comparison when the cathode in found in the lower channel or upper channel at 300 mA cm^{-2}, 0.5 M H_2SO_4 + TritX, (a) 30 mL h^{-1} (b) 40 mL h^{-1} (c) 60 mL h^{-1} (d) 80 mL h^{-1}.

membraneless electrolyzers (TVME) for hydrogen generation. Computational simulations were used to optimize the integrated channels of the TVME in order to increase convective flow and improve the overall efficiency of gas separation.

By introducing a surfactant into the electrolyte, the PE design can operate at 300 mA cm^{-2} and 60 mL h^{-1}. Subsequently, the study proposes a geometry comprising two channels containing electrodes, with connectors designed based on the Tesla valve concept. With this design, diodicity has been used for the first time in membraneless electrolyzer literature. The results indicate that this structure can operate at 300 mA cm^{-2} and 30 mL h^{-1}, staying below the threshold for unsafe cross-contamination of H_2 and O_2. This is the lowest reported required pumping power for the corresponding current density With the addition of the surfactant, the Tesla valve Membraneless Electrolyzer (TVME) is capable of operating at 600 mA cm^{-2} and 80 mL h^{-1} which is matches the highest current density reported under similar conditions in the literature. Moreover, results show that the electrode aided by Tesla valve design and higher flow rate exhibits greater H_2 production frequency. In the proposed structure of TVME, when the cathode is located in the lower channel, it produces with 13% higher frequency of H_2 on the average in comparison when the cathode is positioned in the upper channel. TVME can work more efficient through optimizing the pressure drop and ohmic losses. This study presents the feasible application of the Tesla valve microreactor platform for hydrogen production and thus creates a basis for the scale-up of these microfluidic configurations into larger pilot-scale systems. The results show a promising path toward increasing the technology readiness level (TRL) of such systems, paving the way to move them into feasible, scalable, and efficient renewable energy solutions in the future.

CRediT authorship contribution statement

Mohammadali Zoljalali: Writing – original draft, Software, Investigation, Conceptualization. **Richard Ahorsu:** Writing – review & editing. **Francesc Díaz:** Supervision. **Magdalena Aguiló:** Supervision. **Xavier Mateos:** Writing – review & editing, Supervision, Project administration, Funding acquisition.

Data availability statement

The data that support the findings of this study are available from the corresponding author upon reasonable request.

Funding

This project has received funding from the European Union's Horizon 2020 research and innovation programme under the Marie Skłodowska-Curie Grant Agreement No. 945413 and from the Universitat Rovira i Virgili (URV) under project ID: 2021MFP-COFUND-23-UE. Project PID2022-141499OB-100, funded by MICIU/AEI/10.13039/501100011033/and by FEDER/UE.

Declaration of interests

The authors declare that they have no known competing financial interests or personal relationships that could have appeared to influence the work reported in this paper.

Appendix A. Supplementary data

Supplementary data to this article can be found online at https://doi.org/10.1016/j.ijhydene.2025.02.235.

References

[1] Ehlers JC, Feidenhans'l AA, Therkildsen KT, Larrazábal GO. Affordable green hydrogen from alkaline water electrolysis: key research needs from an industrial perspective. Am Chem Soc Mar. 10, 2023. https://doi.org/10.1021/acsenergylett.2c02897.
[2] Samir De B, Singh A, Ji Dixit R, Khare N, Elias A, Basu S. Hydrogen generation in additively manufactured membraneless microfluidic electrolysis cell: performance evaluation and accelerated stress testing. Chem Eng J 2023;452(Jan). https://doi.org/10.1016/j.cej.2022.139433.
[3] Shiva Kumar S, Himabindu V. Hydrogen production by PEM water electrolysis – a review. KeAi Communications Co; Dec. 01, 2019. https://doi.org/10.1016/j.mset.2019.03.002.
[4] Tashie-Lewis BC, Nnabuife SG. Hydrogen production, distribution, storage and power conversion in a hydrogen economy - a technology review. Elsevier B.V.; Nov. 15, 2021. https://doi.org/10.1016/j.ceja.2021.100172.
[5] Zhao G, et al. Life cycle assessment of H2O electrolysis technologies. Int J Hydrogen Energy Sep. 2020;45(43):23765–81. https://doi.org/10.1016/j.ijhydene.2020.05.282.
[6] Pang X, Davis JT, Harvey AD, Esposito DV. Framework for evaluating the performance limits of membraneless electrolyzers. Energy Environ Sci Oct. 2020; 13(10):3663–78. https://doi.org/10.1039/d0ee02268c.
[7] Yan X, et al. A membrane-free flow electrolyzer operating at high current density using earth-abundant catalysts for water splitting. Nat Commun Dec. 2021;12(1). https://doi.org/10.1038/s41467-021-24284-5.
[8] Manzotti A, Robson MJ, Ciucci F. Recent developments in membraneless electrolysis. Elsevier B.V.; Apr. 01, 2023. https://doi.org/10.1016/j.cogsc.2023.100765.
[9] Zhang D, Zeng K. Evaluating the behavior of electrolytic gas bubbles and their effect on the cell voltage in alkaline water electrolysis. Ind Eng Chem Res Oct. 2012;51(42):13825–32. https://doi.org/10.1021/ie301029e.
[10] Angulo A, van der Linde P, Gardeniers H, Modestino M, Fernández Rivas D. Influence of bubbles on the energy conversion efficiency of electrochemical reactors. Cell Press; Mar. 18, 2020. https://doi.org/10.1016/j.joule.2020.01.005.
[11] Darband GB, Aliofkhazraei M, Shanmugam S. Recent advances in methods and technologies for enhancing bubble detachment during electrochemical water splitting. Elsevier Ltd.; Oct. 01, 2019. https://doi.org/10.1016/j.rser.2019.109300.
[12] Li L, et al. Efficient mesh interface engineering: insights from bubble dynamics in electrocatalysis. ACS Appl Mater Interfaces Sep. 2021;13(38):45346–54. https://doi.org/10.1021/acsami.1c07637.
[13] Khan H, Ullah A, Shin MC, Kwak MK, Kim GM. Effect of electrodes positions on the performance of microfluidic enzymatic biofuel cell: from two streams to a single-stream flow device. Int J Hydrogen Energy Sep. 2021;46(67):33541–50. https://doi.org/10.1016/j.ijhydene.2021.07.153.
[14] Rewatkar P, Bandapati M, Goel S. Miniaturized additively manufactured co-laminar microfluidic glucose biofuel cell with optimized grade pencil bioelectrodes. Int J Hydrogen Energy Nov. 2019;44(59):31434–44. https://doi.org/10.1016/j.ijhydene.2019.10.002.
[15] Rambabu P, Patel S, Gogoi D, Uppaluri RVS, Peela NR. Optofluidic microreactor for the photocatalytic water splitting to produce green hydrogen. Int J Hydrogen Energy Jan. 2022;47(4):2152–63. https://doi.org/10.1016/j.ijhydene.2021.10.171.
[16] Qureshi M, Garcia-Esparza AT, Shinagawa T, Sautet P, Le Bahers T, Takanabe K. Contribution of electrolyte in nanoscale electrolysis of pure and buffered water by particulate photocatalysis. Sustain Energy Fuels 2018;2(9):2044–52. https://doi.org/10.1039/c8se00272j.
[17] Hashemi SMH, et al. A versatile and membrane-less electrochemical reactor for the electrolysis of water and brine. Energy Environ Sci May 2019;12(5):1592–604. https://doi.org/10.1039/c9ee00219g.
[18] Torii K, Kodama M, Hirai S. Three-dimensional coupling numerical simulation of two-phase flow and electrochemical phenomena in alkaline water electrolysis. Int J Hydrogen Energy Oct. 2021;46(71):35088–101. https://doi.org/10.1016/j.ijhydene.2021.08.101.
[19] Manzotti A, Quattrocchi E, Curcio A, Kwok SCT, Santarelli M, Ciucci F. Membraneless electrolyzers for the production of low-cost, high-purity green hydrogen: a techno-economic analysis. Energy Convers Manag 2022;254(Feb). https://doi.org/10.1016/j.enconman.2021.115156.
[20] Rajaei H, Rajora A, Haverkort JW. Design of membraneless gas-evolving flow-through porous electrodes. J Power Sources 2021;491(Apr). https://doi.org/10.1016/j.jpowsour.2020.229364.
[21] Hashemi SMH, Modestino MA, Psaltis D. A membrane-less electrolyzer for hydrogen production across the pH scale. Energy Environ Sci Jul. 2015;8(7): 2003–9. https://doi.org/10.1039/c5ee00083a.
[22] Razavi Bazaz S, Mashhadian A, Ehsani A, Saha SC, Krüger T, Ebrahimi Warkiani M. Computational inertial microfluidics: a review. Royal Society of Chemistry; Mar. 21, 2020. https://doi.org/10.1039/c9lc01022j.
[23] Shi R. Numerical simulation of inertial microfluidics: a review. Taylor and Francis Ltd; 2023. https://doi.org/10.1080/19942060.2023.2177350.
[24] Hadikhani P, Hashemi SMH, Psaltis D. The impact of surfactants on the inertial separation of bubbles in microfluidic electrolyzers. J Electrochem Soc Sep. 2020; 167(13):134504. https://doi.org/10.1149/1945-7111/abb6ca.
[25] Hadikhani P, et al. Inertial manipulation of bubbles in rectangular microfluidic channels. Lab Chip Apr. 2018;18(7):1035–46. https://doi.org/10.1039/c7lc01283g.
[26] Kempler PA, Coridan RH, Luo L. Gas evolution in water electrolysis. Am Chem Soc 2024. https://doi.org/10.1021/acs.chemrev.4c00211.
[27] Hadikhani P, Hashemi SMH, Schenk SA, Psaltis D. A membrane-less electrolyzer with porous walls for high throughput and pure hydrogen production. Sustain Energy Fuels May 2021;5(9):2419–32. https://doi.org/10.1039/d1se00255d.
[28] Hadikhani P, Hashemi SMH, Psaltis D. The impact of surfactants on the inertial separation of bubbles in microfluidic electrolyzers. J Electrochem Soc Sep. 2020; 167(13):134504. https://doi.org/10.1149/1945-7111/abb6ca.
[29] Nobakht AY, Shahsavan M, Paykani A. Numerical study of diodicity mechanism in different tesla-type microvalves. J Appl Res Technol 2013;11(6):876–85. https://doi.org/10.1016/S1665-6423(13)71594-3.
[30] Liu Z, Shao WQ, Sun Y, Sun BH. Scaling law of the one-direction flow characteristics of symmetric Tesla valve. Eng.Appl.Computat. Fluid Mech. 2022;16 (1):441–52. https://doi.org/10.1080/19942060.2021.2023648.
[31] Struyven F, Sellier M, Mandin P. Review: Interactions between electrogenerated bubbles and microfluidic phenomena. Elsevier Ltd.; Oct. 05, 2023. https://doi.org/10.1016/j.ijhydene.2023.04.333.
[32] Pang X, Davis JT, Harvey AD, Esposito DV. Framework for evaluating the performance limits of membraneless electrolyzers. Energy Environ Sci Oct. 2020; 13(10):3663–78. https://doi.org/10.1039/d0ee02268c.
[33] Manzotti A, Quattrocchi E, Curcio A, Kwok SCT, Santarelli M, Ciucci F. Membraneless electrolyzers for the production of low-cost, high-purity green hydrogen: a techno-economic analysis. Energy Convers Manag 2022;254(Feb). https://doi.org/10.1016/j.enconman.2021.115156.
[34] Li Y, et al. In-situ investigation and modeling of electrochemical reactions with simultaneous oxygen and hydrogen microbubble evolutions in water electrolysis. 2019.
[35] Bikerman JJ. Surface chemistry. 1958.
[36] Hadikhani P, Hashemi SMH, Schenk SA, Psaltis D. A membrane-less electrolyzer with porous walls for high throughput and pure hydrogen production. Sustain Energy Fuels May 2021;5(9):2419–32. https://doi.org/10.1039/d1se00255d.
[37] Zhao X, Ren H, Luo L. Gas bubbles in electrochemical gas evolution reactions. Langmuir Apr. 2019;35(16):5392–408. https://doi.org/10.1021/acs.langmuir.9b00119.
[38] Purwidyantri A, Prabowo BA. Tesla valve microfluidics: the rise of forgotten technology. Multidisciplinary Digital Publishing Institute (MDPI); Apr. 01, 2023. https://doi.org/10.3390/chemosensors11040256.
[39] The Mixture Model, Laminar flow interface.".
[40] Rajora A, Haverkort JW. An analytical model for the velocity and gas fraction profiles near gas-evolving electrodes. Int J Hydrogen Energy Aug. 2023;48(71): 27450–63. https://doi.org/10.1016/j.ijhydene.2023.03.154.
[41] Rajora A, Haverkort JW. An analytical multiphase flow model for parallel plate electrolyzers. Chem Eng Sci Oct. 2022;260. https://doi.org/10.1016/j.ces.2022.117823.
[42] Du G, et al. Improving thermal and hydraulic performances through artificial neural networks: an optimization approach for Tesla valve geometrical parameters. Case Stud Therm Eng Dec. 2023;52. https://doi.org/10.1016/j.csite.2023.103670.
[43] Hacha RR, Merma AG, Couto HJB, Torem ML. Measurement and analysis of H2 and O2 bubbles diameter produced by electroflotation processes in a modified

Partridge-Smith cell. Powder Technol Jan. 2019;342:308–20. https://doi.org/10.1016/j.powtec.2018.09.062.
[44] Liu Y, Li S, Wu H, Shi Y. Experimental investigation and analysis for the bubble size distribution during alkaline water electrolysis by using a wire electrode. DeCarbon Sep. 2024;5:100052. https://doi.org/10.1016/j.decarb.2024.100052.
[45] Li Y, et al. In-situ investigation and modeling of electrochemical reactions with simultaneous oxygen and hydrogen microbubble evolutions in water electrolysis. 2019.
[46] Hadikhani P. Investigating bubble-induced overpotential, current non-uniformity, and bubble distribution in flow-based water electrolyzers: a numerical study. Int J Hydrogen Energy Sep. 2024;84:793–802. https://doi.org/10.1016/j.ijhydene.2024.08.231.
[47] Colclasure AM, et al. Electrode scale and electrolyte transport effects on extreme fast charging of lithium-ion cells. Electrochim Acta 2020;337(Mar). https://doi.org/10.1016/j.electacta.2020.135854.